ALMA-IMF. IV. A comparative study of the main hot cores in W43-MM1: Detection, temperature, and molecular composition

N. Brouillet, D. Despois, J. Molet, T. Nony, F. Motte, A. Gusdorf, F. Louvet, S. Bontemps, F. Herpin, M. Bonfand, et al.

A&A 665, A140 (2022)
https://doi.org/10.1051/0004-6361/202243669

Astronomy & Astrophysics

ALMA-IMF

IV. A comparative study of the main hot cores in W43-MM1: Detection, temperature, and molecular composition

N. Brouillet[1], D. Despois[1], J. Molet[1], T. Nony[2], F. Motte[3], A. Gusdorf[4,5], F. Louvet[3,6], S. Bontemps[1], F. Herpin[1], M. Bonfand[1], T. Csengeri[1], A. Ginsburg[7], N. Cunningham[3], R. Galván-Madrid[2], L. Maud[8], G. Busquet[9,10,11], L. Bronfman[12], M. Fernández-López[13], D. L. Jeff[7], B. Lefloch[3], Y. Pouteau[3], P. Sanhueza[14,15], A. M. Stutz[16], and M. Valeille-Manet[1]

(Affiliations can be found after the references)

Received 29 March 2022 / Accepted 27 June 2022

ABSTRACT

Context. Hot cores are signposts of the protostellar activity of dense cores in star-forming regions. W43-MM1 is a young region that is very rich in terms of high-mass star formation, which is highlighted by the presence of large numbers of high-mass cores and outflows.
Aims. We aim to systematically identify the massive cores in W43-MM1 that contain a hot core and compare their molecular composition.
Methods. We used Atacama Large Millimeter/sub-millimeter Array (ALMA) high-spatial resolution (~2500 au) data to identify line-rich protostellar cores and carried out a comparative study of their temperature and molecular composition. Here, the identification of hot cores is based on both the spatial distribution of the complex organic molecules and the contribution of molecular lines relative to the continuum intensity. We rely on the analysis of CH_3CN and CH_3CCH to estimate the temperatures of the selected cores. Finally, we rescale the spectra of the different hot cores based on their CH_3OCHO line intensities to directly compare the detections and line intensities of the other species.
Results. W43-MM1 turns out to be a region that is rich in massive hot cores. It contains at least one less massive (core #11, 2 $M_\odot$) and seven massive (16–100 $M_\odot$) hot cores. The excitation temperature of CH_3CN, whose emission is centred on the cores, is of the same order for all of them (120–160 K). There is a factor of up to 30 difference in the intensity of the lines of complex organic molecules (COMs). However the molecular emission of the hot cores appears to be the same or within a factor of 2–3. This suggests that these massive cores, which span about an order of magnitude in core mass, have a similar chemical composition and show similar excitation of most of the COMs. In contrast, CH_3CCH emission is found to preferentially trace the envelope, with a temperature ranging from 50 K to 90 K. Lines in core #11 are less optically thick, which makes them proportionally more intense compared to the continuum than lines observed in the more massive hot cores. Core #1, the most massive hot core of W43-MM1, shows a richer line spectrum than the other cores in our sample, in particular in N-bearing molecules and ethylene glycol lines. In core #2, the emission of O-bearing molecules, such as OCS, CH_3OCHO, and CH_3OH, does not peak at the dust continuum core centre; the blueshifted and redshifted emission corresponds to the outflow lobes, suggesting formation via sublimation of the ice mantles through shocks or UV irradiation on the walls of the cavity. These data establish a benchmark for the study of other massive star-formation regions and hot cores.

Key words. stars: formation – stars: massive – ISM: abundances – ISM: molecules – radio lines: ISM

1. Introduction

W43-MM1 is a massive star-formation region 5.5 kpc away (Zhang et al. 2014) and located at the tip of the Galactic bar (Nguyen Luong et al. 2011). Among the 131 cores with typical sizes of 2000 au identified by Motte et al. (2018; hereafter M18) using Atacama Large Millimeter/sub-millimeter Array (ALMA) data, 18 have masses >10 $M_\odot$. The large number of massive cores detected in W43-MM1 make it an ideal laboratory for exploring the physical processes and chemical evolution involved in the formation of massive stars.

The identification of massive cores in W43-MM1 and the characterisation of their environment results from many years of sustained effort involving observations and state-of-the-art simulations and models. Motte et al. (2003) found such a high star-formation rate and efficiency in W43 that they deemed this region a 'mini-starburst', reminiscent of the galaxies referred to as such. *Herschel* and ground-based observations revealed a complex structure of molecular filaments hosting dense cores exposed to the radiation from neighbouring massive stars (Bally et al. 2010; Cortes et al. 2010; Cortes 2011; Nguyen Luong et al. 2011; Nguyen-Luong et al. 2013, 2017; Carlhoff et al. 2013). Herpin et al. (2009, 2012) studied the water emission from the W43-MM1 dense filament, and found a very turbulent and infalling medium, and inferred a high accretion luminosity. Louvet et al. (2014) used NOrthern Extended Millimeter Array (NOEMA) observations of the dust continuum emission in W43-MM1 with a typical angular resolution of 3″ to highlight a linear correlation between the star formation efficiencies and the density in different layers of the filament. Louvet et al. (2016) used the same dataset together with grids of models provided by the Paris-Durham shock model (Gusdorf et al. 2015, 2017) to characterise the ongoing shock processes. These authors showed that the filament was probably the result of

Table 1. Parameters of the 3 mm and 1.3 mm ALMA spectral windows.

Spectral	Bandwidth	Resolution		rms	
windows	(GHz)	($'' \times ''$)	(km s^{-1})	(K)	(mJy beam^{-1})
Band 3					
spw0	93.089–93.200	0.60×0.39	1.57	1.00	1.6
spw1	91.703–92.637	0.61×0.39	1.59	0.60	1.0
spw2	102.100–103.035	0.57×0.36	1.43	0.70	1.2
spw3	104.500–105.435	0.57×0.35	1.39	0.60	1.1
Band 6					
spw0	216.015–216.248	0.55×0.40	0.17	0.37	3.1
spw1	216.965–217.197	0.54×0.39	0.34	0.42	3.4
spw2	219.809–219.933	0.54×0.39	0.33	0.44	3.7
spw3	218.036–218.278	0.54×0.39	0.17	0.38	3.1
spw4	219.424–219.549	0.53×0.39	0.17	0.49	4.0
spw5	230.226–230.684	0.52×0.38	1.27	0.25	2.1
spw6	230.973–231.439	0.52×0.37	0.32	0.28	2.3
spw7	232.492–234.360	0.51×0.36	1.26	0.22	1.8
cycle3	231.432–233.300	0.66×0.50	1.26	0.12	1.7

Notes. The wide Band 6 spw7 spectral window is also referred to as the 'continuum' band.

a cloud–cloud collision, and revealed the presence of numerous bipolar outflows. In the meantime, Sridharan et al. (2014) confirmed the presence of dense cores with the Submillimeter Array (SMA) and revealed local variations of the magnetic field. Cortes et al. (2016) studied the magnetic field structure at ~0.5″ resolution.

ALMA observations revolutionised our understanding of this region: M18 identified and characterised 131 pre- and protostellar cores in the region at ~0.5″ resolution, measuring their mass, temperature, size, and density, and obtaining an unexpected core mass function (CMF) with an excess of massive cores. Nony et al. (2018) studied the physical structure of the remarkably massive (~55 $M_\odot$ in 1300 au radius) pre-stellar core candidate (core #6) found in the region, while its chemistry was studied by Molet et al. (2019). Nony et al. (2020) investigated the ejection–accretion link by studying the characteristics of 46 molecular outflow lobes identified with ALMA and found evidence for time-variable ejection processes with a timescale of ~ 500 yr.

The large program 'ALMA-IMF: ALMA transforms our view of the origin of stellar masses' (project # 2017.1.01355.L; Ginsburg et al. 2022; Motte et al. 2022; Pouteau et al. 2022) extends the work by M18 that found the first 'top-heavy' CMF in the W43-MM1 protocluster. ALMA-IMF consists of the observation of 15 massive protoclusters to investigate the distribution of the 0.5–200 $M_\odot$ cores at a ~2000 au scale and thus characterise the CMF evolution. Another aim of the program is to determine the pre-stellar, protostellar, or UCHII region nature of the cores.

In this paper we focus on the identification and characterisation of the hot cores in W43-MM1. By analogy with the Orion hot core (e.g. Morris et al. 1980), a hot core is usually defined as a hot ($T \geq 100$ K), dense (density $\geq 10^6$ cm^{-3}), and compact (diameter <0.1 pc) region where a large number of molecular lines from complex organic molecules (COMs) are detected (e.g. Cesaroni et al. 1994; Herbst & van Dishoeck 2009; Charnley 2011). The study of the chemistry of star-forming regions can provide us with precious information on the physical evolution of protostars (e.g. Jørgensen et al. 2020).

The present article is organised as follows. We present our data in Sect. 2. In Sect. 3, we identify eight hot cores with two methods: one using the spatial distribution of molecules and the other one using the line densities compared to the continuum level in the continuum cores, and we confirm the nature of these cores using methyl formate and methyl cyanide maps. In Sect. 4, we determine the temperature of the hot cores from the CH_3CN and CH_3CCH emission. In Sect. 5, we compare the molecular composition of the hot cores from their spectra normalised to the intensities of the methyl formate lines. We discuss the molecular similarity of the hot cores using scaled spectra and correlation plots in Sect. 6. Our conclusions are presented in Sect. 7.

2. Observations

We use band 3 and band 6 ALMA observations of W43-MM1 carried out between 2014 and 2018. The 1.3 mm observations (216 to 234 GHz) are from ALMA Cycle 2 (project #2013.1.01365.S) and Cycle 3 (#2015.1.01273.S) and were previously presented in Molet et al. (2019), together with our continuum-subtraction method. The 1.3 mm dataset is composed of nine bands of bandwidths between 0.1 and 1.9 GHz, with a spatial resolution of ~0.45″, a spectral resolution ranging from 0.2 to 1.3 km s^{-1} and an rms between 0.1 and 0.5 K (see Table 1). The observations are 2.1 pc × 1.4 pc mosaics taken with the ALMA 12 m and ACA 7 m arrays. The gridding was performed with Briggs' weighting using a robustness parameter of 0.5, and the cleaning used the multiscale option excluding the borders of the mosaic to avoid divergence problems. Hence, between 120 and 129 of the 131 cores of M18 are in the cleaned field, depending on the band.

The 3 mm observations (91.7–105.4 GHz) are from ALMA Cycle 5 and are part of the large program ALMA-IMF. This program covered the W43-MM1 region at 3 mm at a comparable resolution to the previous 1 mm data. In this paper, we present a preliminary data reduction and analysis of these 3 mm data. We use the same cleaning and continuum subtraction method (based on the distribution of channel intensities) as presented in

Molet et al. (2019), using CASA[1]. Cunningham et al. (in prep.) present the standardised data reduction methods applied by the ALMA-IMF consortium to homogenise the analysis of all the regions observed. On average, the observational parameters for the four selected bands have a spatial resolution of 0.46″ (2500 au), a spectral resolution of 1.5 km s^{-1} (0.5 MHz), and an rms of 0.6 K per channel; the detailed parameters for each band are given in Table 1. These bands include several lines of CH_3CN (spw1), CH_3CCH (spw2), and CH_3OH (spw3).

We also made 1.3 mm maps with a higher spatial resolution – applying a uniform weighting to visibilities in the gridding – in order to study the distribution of the molecules in Sect. 5.2. We reached a resolution that is 1.5 times better (0.3″ or 1600 au) at the expense of a lower sensitivity.

The conversion from flux density to brightness temperature was made using the formula[2]:

$$T = 1.222 \times 10^3 \frac{I}{\nu^2 \theta_{\rm maj} \theta_{\rm min}}, \quad (1)$$

where T is the brightness temperature, I the flux in mJy beam^{-1}, ν the frequency in GHz, and $\theta_{\rm maj}$ and $\theta_{\rm min}$ are the half-power beam widths along the major and minor axes, respectively.

3. Identification of hot cores

To identify hot cores, we used two different approaches, one that uses molecules known to trace hot cores (see Sect. 3.5) and another one that does not need any line identification and relies on the richness of the hot core spectra in COM lines. Two methods based on this latter approach are presented in Sect. 3.3 and Sect. 3.4. The first one is based on the sum of the brightness temperature of all lines over the Band 6 spw7 band; this sum is computed for each pixel of a 2500 au spatial resolution map, and requires no prior knowledge of the region. The selected band is particularly rich in COM lines. The second one is based on the sum over a band of the line contribution averaged over the area of a continuum core and compared to the continuum emission. We use the different bands from Table 1 (bandwidth between 0.1 and 2 GHz). We study first the brightness temperature of the line emission to estimate the 'contamination' of the continuum emission by line emission, and then simply the number of lines detected to get the 'density in lines', which is the fraction of the band showing detected lines. This method requires identification of the continuum cores as a first step.

We note that, as indicated in Sect. 2, up to 11 of the 131 cores from M18 are out of the bounds of our data cubes. Specifically, this is the case for cores #15, #39, #44, #59, and #67 located in W43-MM1 SW, all of which are associated with molecular outflows (Nony et al. 2020). Among these cores, M18 indicated that only core #15 has detectable molecular lines. None of these are included in the analysis that follows.

3.1. Continuum level

We separated the continuum and the molecular emission in each pixel of the image using the method presented in Molet et al. (2019). The continuum level is estimated from the spectrum intensity channel distribution, after fitting it with an exponentially modified Gaussian to adjust both the Gaussian distribution of the noise and the asymmetric distribution of the lines intensities (see Fig. 1).

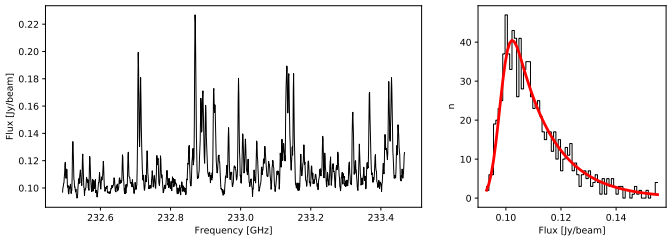

Fig. 1. *Left*: spectrum with molecular line emission in the Band 6 spw7 band. *Right*: distribution of the intensity channels (in black). An exponentially modified Gaussian (in red) is adjusted to fit the Gaussian part due to the noise, whose peak is taken as the continuum value, and the tail associated with the molecular emission.

3.2. Indicators of richness in lines

To quantify the line richness, we take the line brightness temperature at a pixel or average it over a given spatial region R, and sum it on individual channels over a given frequency range, and refer to the integrated line emission as $I^{\rm pix}_{\rm Lines}$ and $I^{\rm R}_{\rm Lines}$, respectively.

$$I^{\rm pix}_{\rm Lines} = \sum_i^{n_{\rm chan}} T^{\rm pix}_{{\rm Lines},i} \Delta\nu \text{ and } I^{\rm R}_{\rm Lines} = \sum_i^{n_{\rm chan}} < T_{{\rm Lines},i} >_{\rm R} \Delta\nu, \quad (2)$$

where $T_{{\rm Lines},i}$ is the brightness temperature due to the lines in channel i; it is computed using the total brightness temperature $T_{{\rm Total},i}$ and the continuum value $T_{\rm Cont}$ determined previously:

$$T_{{\rm Lines},i} = T_{{\rm Total},i} - T_{\rm Cont}, \quad (3)$$

$<>_{\rm R}$ indicates the average of the line brightness temperature over the spatial region R, $n_{\rm chan}$ is the number of channels, and $\Delta\nu$ is the channel width.

3.3. Hot core identification from the spatial distribution of COMs

To highlight the presence of hot cores, we focus on the analysis of the 'continuum' band (spw7) at 233 GHz, because this band offers a large band width (~2 GHz) that is not contaminated by strong emission lines coming from the simplest molecules (like H_2CO, CO or SiO) but mainly by COMs. Moreover, M18 and Molet et al. (2019) have already studied the 233 GHz band towards W43-MM1.

For each pixel we compute the integrated line emission $I^{\rm pix}_{\rm Lines}$ and divide by the number of channels ($T^{\rm pix}_{\rm Lines} = I^{\rm pix}_{\rm Lines}/n_{\rm chan}$) to produce the mean line brightness temperature map in Fig. 2. Similarly, using the total channel intensity and the continuum contribution, we obtain maps of $T^{\rm pix}_{\rm Total}$ and $T^{\rm pix}_{\rm Cont}$ which are also shown in the same figure. We assume that the continuum intensity does not vary significantly over the spectral band ($\Delta\nu$ = 1.9 GHz), the expected difference being only 2% in this range of frequency.

Because the continuum emission is bright at 1.3 mm, the structures in the total integrated map are very similar to the ones found in the continuum map. To reveal the presence of hot cores, we look on the map for places where line emission $T^{\rm pix}_{\rm Lines}$ is greater than the noise (first 3 sigma contour in Fig. 2). With

[1] https://casa.nrao.edu
[2] https://science.nrao.edu/facilities/vla/proposing/TBconv

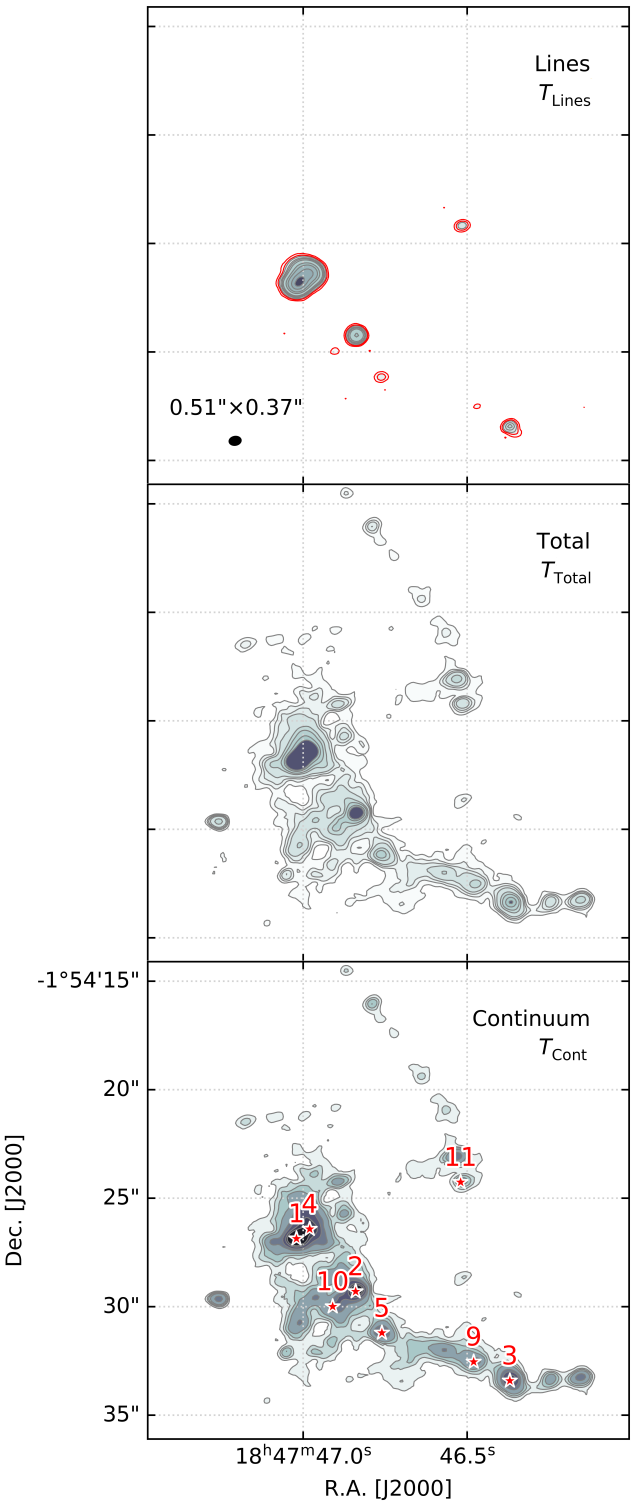

Fig. 2. Lines, and total and continuum emission maps obtained from the spw7 band at 233 GHz. Contours represent 3, 5, 7, 10, 20, 30, 50, 70, and 100 σ, with σ = 0.22 K, the rms in a channel of resolution $\Delta\nu$ = 0.122 MHz. The hot cores are marked by a star symbol. The total emission is averaged over the 1.9 GHz band. For the line map, the first two contours are added in red to reveal the fainter hot cores.

this method, seven structures are highlighted, among which the largest one previously identified as N1a, detected at 5″ × 3″ resolution with NOEMA (Louvet et al. 2014), and separated into two substructures at 2400 au resolution with ALMA (Motte et al. 2018; Nony et al. 2020). The centre of these eight structures

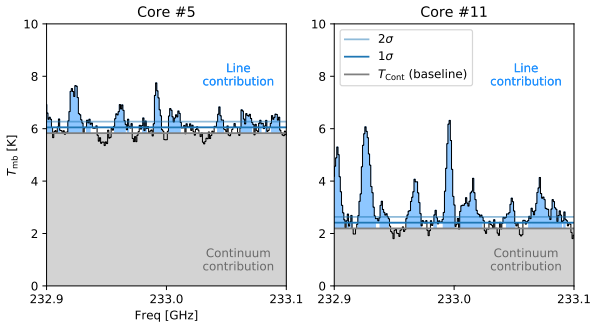

Fig. 3. Separation of continuum and line contributions for cores #5 and #11 as examples. The spectra are spatially averaged over the source size. The grey horizontal line across the observed spectra (in black) is the continuum level obtained by the method of Molet et al. (2019). Below this line, the grey area represents the continuum integrated flux. Above this line, the blue area is the continuum brightness of the lines, which is estimated in each channel depending on the noise, whose 1σ and 2σ values are represented by horizontal lines.

is in agreement with the position of eight of the brightest continuum cores identified by M18 and marked on the continuum map: cores #1, #2, #3, #4, #5, #9, #10 and #11, with structures #1 and #4 contributing to one (possibly double) hot core candidate in the line map. All of them are high-mass cores (16–102 $M_\odot$, see M18) located on the main filament, except core #11 (2 $M_\odot$).

The spectra of the other cores identified by M18 do not show any lines in this band or the lines are not bright enough for the comparative line methods discussed in Sects. 4 and 5. The detected lines are individually not significant enough for a clear constraint of line parameters (shape, centre, and width) and therefore the uncertainties on physical parameters such as temperature and column densities are too high. Nonetheless, a detailed previous study showed that we can analyse the same lines in the sources of W43-MM1 with the faintest 1.3 mm line, such as core #6, which is a high-mass prestellar or very young protostellar core. A complete analysis of the spectra from cores #3 and #6 can be found in Molet et al. (2019). A direct analysis for cores #1 and #4 is difficult because they appear to be interacting and affected by significant spectral confusion.

3.4. Hot core identification from the line densities in continuum cores

As M18 have already identified the continuum cores in the W43-MM1 region and defined their sizes and locations, we propose another method to highlight the cores that contain a hot core. Unlike the pixel-based analysis in Sect. 3.3, we look for the relative contributions of continuum and molecular line emission in the spectra of the continuum cores, spatially integrated over the source size given by M18.

For each spectrum, we distinguish channels with molecular emission from line-free (or continuum) channels by verifying whether the core total intensity $T^{\rm core}_{{\rm Total},i}$ of the channel i – once the continuum is subtracted – is above or below 1σ (the rms measured in a line free part of the spectra), respectively (see Fig. 3). After tests on synthetic spectra, we find that the contribution of the lines is better taken into account if we consider all the line signal for a channel with an intensity greater than 2σ, and only signal above 1σ for a channel with an intensity of between 1σ and 2σ.

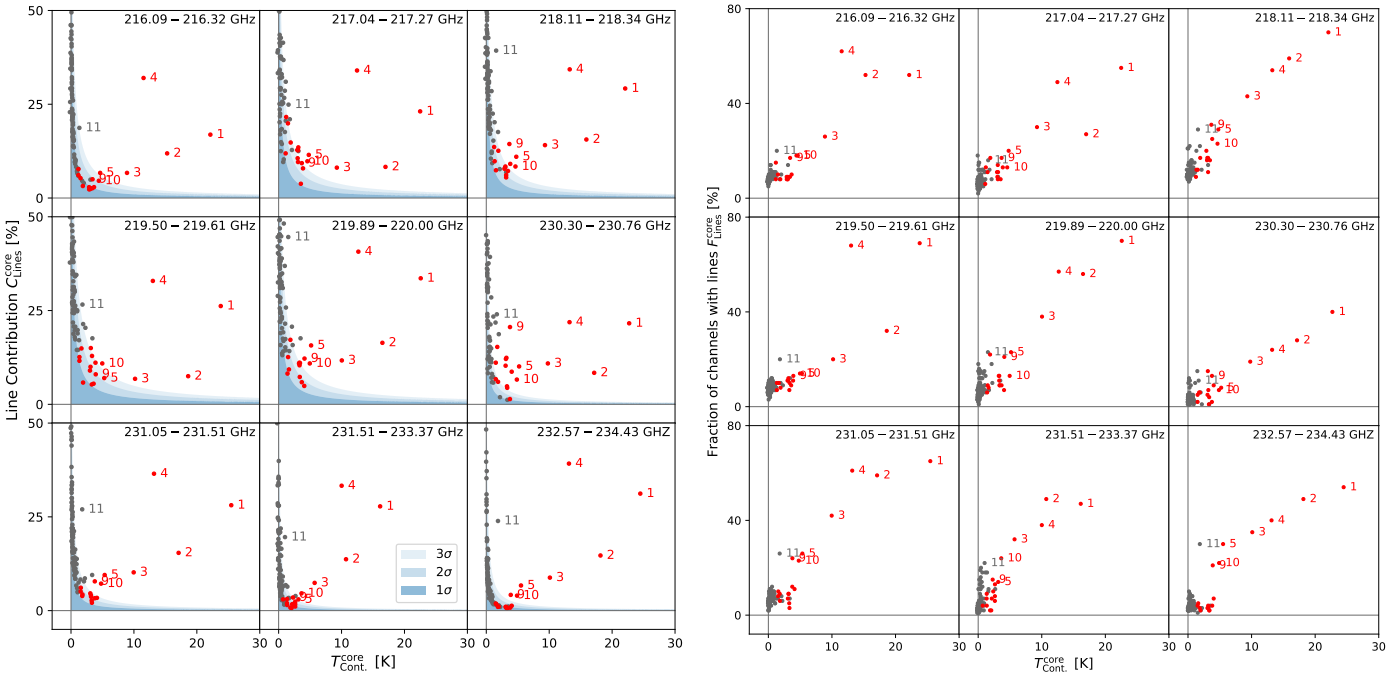

Fig. 4. Relative line contribution to the total flux (*left*) and fraction of channels that contain molecular emission (*right*) as a function of the continuum level obtained for the 1.3 mm bands. Red dots represent high-mass cores with $M > 10\,M_\odot$, grey dots represent the other cores. The blue areas represent the results for spectra without many lines above the 1σ, 2σ, and 3σ levels, where σ is the rms noise level in one channel of the corresponding band. Cores identified as containing a hot core following the criterion described in Sect. 1 are marked by their core number.

Therefore, for a core spectrum, we define the line contribution C^{core}_{Lines} to the total brightness as

$$C^{core}_{Lines} = I^{core}_{Lines}/I^{core}_{Total}, \tag{4}$$

and using Eq. 2:

$$C^{core}_{Lines} = \sum_{i}^{n_{chan}} \frac{1}{T^{core}_{Total,\,i}} \times \begin{cases} 0 & \text{if } T^{core}_{Lines,\,i} \leq 1\sigma \\ (T^{core}_{Lines,\,i} - \sigma) & \text{if } 1\sigma < T^{core}_{Lines,\,i} \leq 2\sigma \\ T^{core}_{Lines,\,i} & \text{if } T^{core}_{Lines,\,i} > 2\sigma \end{cases}. \tag{5}$$

The left panel of Fig. 4 presents, for the nine 1.3 mm ALMA bands, the relative contribution C^{core}_{Lines} of lines to the total flux versus T^{core}_{Cont} for all cores. We note that the rapid increase in the relative line contribution at low continuum values corresponds to the cores fainter in lines, for which the method is biased by the noise (blue areas). However, as in Sect. 3.3, cores #1, #2, #3, #4, #5, #9, #10, and #11 clearly stand out. The results are consistent between the bands but the difference between the cores is more obvious for the bands with no strong line (e.g., at 216 GHz), as the strong lines come from molecules which are widespread; the difference is also better in bands with a large frequency range (e.g. the three bands from 231 to 234 GHz).

To avoid the confusion observed for the weak continuum values, another approach using the same method is to focus on the fraction F^{core}_{Lines} of channels considered as containing lines detected at a 2σ level, defined as:

$$F^{core}_{Lines} = \frac{1}{n_{chan}} \times \sum_{i}^{n_{chan}} \begin{cases} 0 & \text{if } T^{core}_{Lines,\,i} \leq 2\sigma \\ 1 & \text{if } T^{core}_{Lines,\,i} > 2\sigma \end{cases}. \tag{6}$$

The results are presented in the right panel of Fig. 4. The relative comparison highlights the same eight cores and we also observe a relation between the number of channels with molecular emission and the continuum level; this correlation is clearer than in the left panel for all bands, even for the 'CO' 230.30–230.76 GHz band.

3.5. Identification from the spatial distribution of CH_3OCHO and CH_3CN

Methyl formate (CH_3OCHO) and methyl cyanide (CH_3CN) are two abundant COMs and are therefore often used to trace hot cores (e.g. Blake et al. 1987; Wink et al. 1994, see also Sect. 5.2). We used Eq. 2 to integrate the line emission at each pixel and Fig. 5 presents maps of the two molecules using the CH_3OCHO doublet at 216.21 GHz (see Sect. 5) and the CH_3CN transitions from 91.958 to 91.987 GHz (see Sect. 4). The methyl formate map highlights the eight hot cores identified on Fig. 2. These hot cores also stand out in the methyl cyanide map but they are surrounded by more widespread extended emission. Such extended CH_3CN emission was also observed in DR21(OH) by Csengeri et al. (2011) who proposed that it traces warm gas associated with the low-velocity shocks due to converging flows coinciding with velocity shears. In W43-MM1, the extended CH_3CN emission follows the spatial distribution of the narrow line width component of the SiO emission which originates from low-velocity shocks (Louvet et al. 2016, see their left panel of Fig. 4). These shocks are also likely associated with the ridge formation through colliding flows or cloud–cloud collision.

3.6. Comparison of the methods used here to identify hot cores

The two methods described in Sects. 3.3 and 3.4 succeed in identifying the same hot cores. The interest of using only the spatial distribution of COMs is that it allows the user to identify

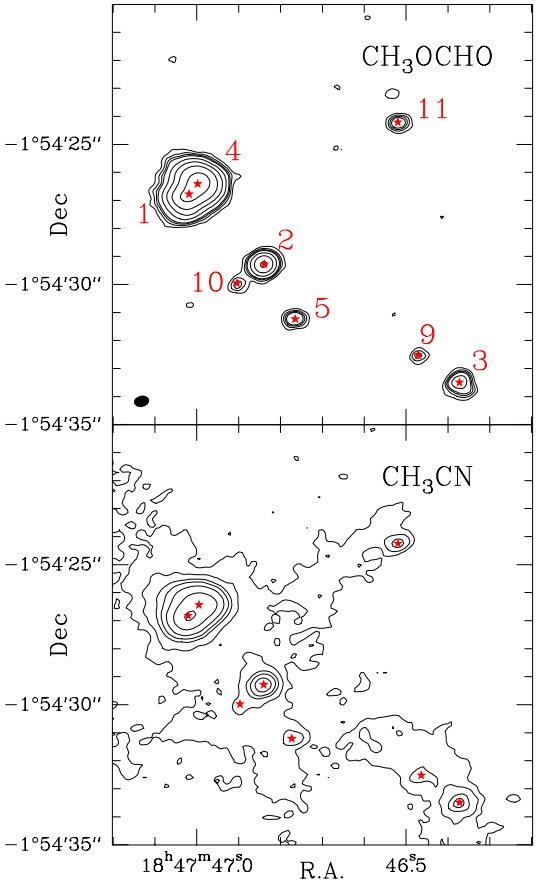

Fig. 5. *Top*: methyl formate intensity map integrated over the velocity (bandwidth of 25 km s^{-1} around the 216.21 GHz transitions). The contours correspond to 3, 6, 9, 12, 24, 50, 100, and 200 σ, where the rms noise σ = 2.6 K km s^{-1}. *Bottom*: Methyl cyanide intensity map integrated over the velocity (bandwidth of 120 km s^{-1} around the 91.97 GHz transitions). The contours correspond to 5, 10, 20, 30, 50, 100, and 200 σ, where the rms noise σ = 83 K km s^{-1}. The red stars indicate the position of the hot cores identified on Fig. 2.

potential hot cores independently of the identification of the continuum cores. However, a spectral band is required that has lines mainly coming from COMs, as in the Band 6 spw7 band, and the sensitivity will be limited by the width of the spectral band and the number of strong COM lines therein.

The second set of methods based on the relative contribution of lines $C^{\rm core}_{\rm Lines}$ with respect to the continuum emission or the fraction $F^{\rm core}_{\rm Lines}$ of channels with detected line emission needs first to identify the continuum cores, and the catalog of continuum cores will depend on the software package used for extraction (see e.g. Pouteau et al. 2022). M18 also identified potential hot cores from the line contamination in the emission of the continuum cores. These authors compared the fluxes measured in a 1.9 GHz 'continuum' band and in a selection of line-free channels summing up to 65 MHz and found the same eight cores as in Sect. 3.4. However, they detected two more cores: core #15 which is not included in our analysis and core #30 which does not display any COM lines when looking at the spectra.

The method used in Sect. 3.5 directly uses hot core tracers. However, it requires first to identify the lines and to be sure that these lines are not blended with other species, which is often the case in hot cores. Furthermore, one needs to determine the velocity of the cores to centre the map on the emission line. When the field of view is large, there is a velocity gradient that makes it more difficult to make a map: one can make a 'composite' map, adapting the velocity throughout the field, or one can take a large velocity window to integrate the emission but the sensibility will be less and the risk of blending lines will be higher. In the case of methyl cyanide, we have also noted that extended emission is also present, which makes it more difficult to identify the faintest hot cores.

4. Core temperatures

Methyl cyanide (CH_3CN) and methyl acetylene (CH_3CCH) are considered as two good thermometers, as long as the lines are optically thin, because their emission K-ladder lines are close in frequency and cover a large enough range of upper level energies $E_{\rm u}$ (see e.g. Giannetti et al. 2017).

4.1. CH_3CN

There are five lines of CH_3CN (J = 5–4) between 91.95 and 91.99 GHz, with upper level energies $E_{\rm u}$ ranging from 13 to 128 K. CH_3CN (5_0–4_0) and CH_3CN (5_1–4_1) are only separated by 2.3 MHz, and because of the average line width of 5 km s^{-1}, these two lines are blended. In the same ALMA spectral window, there are also five lines of the isotopolog $CH_3^{13}CN$ (J = 5–4) with the same $E_{\rm u}$ ranging from 13 to 128 K, as well as ten CH_3CN (J = 5–4) v_8 = 1 lines with $E_{\rm u}$ ranging from 532 to 706 K. The spectroscopic parameters of the lines are given in Table 3.

The CH_3CN and $CH_3^{13}CN$ spectra averaged over the beam for the eight cores are plotted in Fig. 6. The pattern of the CH_3CN lines is similar for all the cores, except for cores #1, #2, #3, and #4, where the five lines are almost equally intense because of line opacity. Nonetheless, the relative intensities of the optically thin lines of the isotopologue $CH_3^{13}CN$ of these four cores are the same as the optically thin CH_3CN pattern of the other cores. The similarity of the pattern with lines of different $E_{\rm u}$ suggests an equivalent temperature for all the cores. The CH_3CN v_8 = 1 lines are only detected towards cores #1, #2, #3, #4, and #11 and are marginally detected towards core #5 (see Fig. 7).

For each core in Fig. 6, we overlay a synthetic spectrum considering the temperatures, column densities, line widths, and a source size indicated in Table 2. Due to the high average H_2 density of these cores (3–76 $\times$ 10^8 cm^{-3}, see M18), we consider that all lines are thermalised. The values are obtained with the Monte-Carlo Markov Chain algorithm and the LTE model of the CASSIS software[3] (Vastel et al. 2015). For cores #1, #2, #3, #4, #5, and #11, the temperatures, column densities, and line widths are first derived from a fit to the optically thin $CH_3^{13}CN$ and CH_3CN v_8 = 1 lines assuming a source size equal to the beam (0.49″). The CH_3CN lines are then taken into account to derive the source size. For cores #9 and #10, the parameters are derived from a fit to the optically thin CH_3CN and $CH_3^{13}CN$ lines assuming a source size equal to the beam. We find an isotopic ratio of about 42, consistent with the 40–50 value at 5.5 kpc (Milam et al. 2005). We assume here a simple model with a uniform source and the emission of CH_3CN, $CH_3^{13}CN$, and CH_3CN v_8 = 1 coming from the same region. A more realistic source model will be used in a forthcoming paper.

The temperatures are similar for all the cores, ranging from 120 K to 160 K with uncertainties of ±20 K. The broader line widths for cores #2 and #5 can be due to multiple velocity components as seen in other COM lines (see Sect. 5.2).

[3] http://cassis.irap.omp.eu

Table 2. CH_3CN and CH_3CCH column densities and temperatures towards the hot cores.

Core	CH_3CN				CH_3CCH			
	T_{ex} (K)	N (10^{16} cm^{-2})	Δv (km s^{-1})	size ($''$)	T_{ex} (K)	N (10^{16} cm^{-2})	Δv (km s^{-1})	Size ($''$)
#1	150	80.0	6.0	0.42	90	7.0	5.0	0.45
#2	140	100.0	6.45	0.19	70	2.5	4.0	0.45
#3	140	40.0	5.0	0.13	60	1.2	4.6	0.45
#4	135	46.0	4.5	0.44	70	4.0	3.8	0.45
#5	160	0.5	9.0	0.49	50	0.35	4.5	0.45
#9	120	0.2	5.0	0.49	55	0.5	4.0	0.45
#10	120	0.25	5.0	0.49	70	1.2	4.0	0.45
#11	150	8.4	5.0	0.14	50	0.35	3.5	0.45

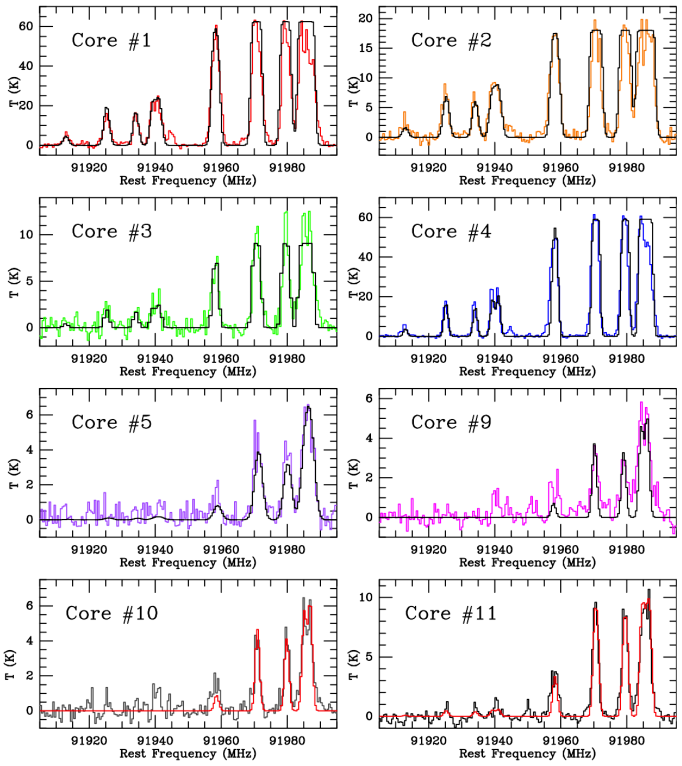

Fig. 6. $CH_3^{13}CN$ (from 91.91 to 91.94 GHz) and CH_3CN (91.95–91.99 GHz) synthetic spectra (in red for cores #10 and #11, in black for the others) overlaid on the observed spectra. The parameters used for the synthetic spectra are listed in Table 2.

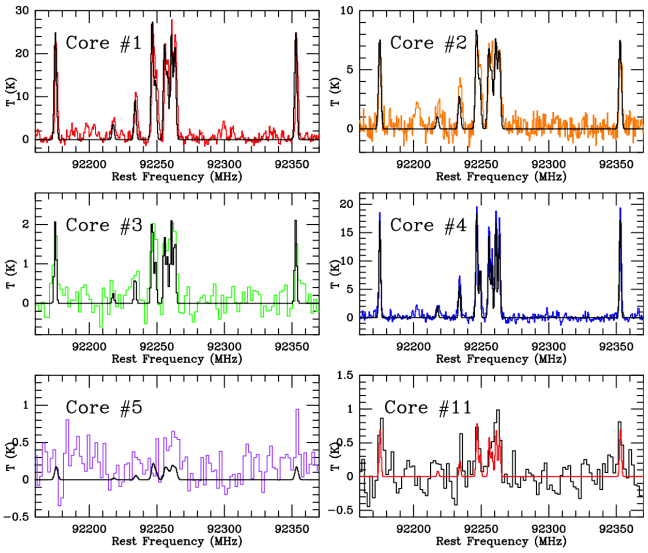

Fig. 7. CH_3CN $v_8 = 1$ synthetic spectra (in red for core #11, in black for the others) overlaid on the observed spectra. The parameters used for the synthetic spectra are listed in Table 2. The spectra for cores #3, #5, and #11 are smoothed to a velocity resolution of 6.35 km s^{-1}.

The CH_3CN transitions are also detected towards the possibly younger core #6 studied by Molet et al. (2019) and the derived temperature is 60 ± 20 K which is in agreement with the determinations in that paper. This temperature is notably different from the temperatures $T_{ex} \sim 150$ K we find here towards the hot cores.

4.2. CH_3CCH

We selected five CH_3CCH (J = 6–5) lines between 102.51 and 102.55 GHz, with upper level energies E_u ranging from 17 to 132 K. CH_3CCH (6_5–5_5) is not studied here, because the line is too weak towards all the cores. As for CH_3CN, the CH_3CCH (6_0–5_0) and CH_3CCH (6_1–5_1) lines are blended, and are also contaminated by acetone (CH_3COCH_3) lines at 102.547 GHz in cores #1, #2, and #4. Furthermore the CH_3CCH (6_2–5_2) line at 102.540 GHz is contaminated by the ethylene glycol, $(CH_2OH)_2$, ($9_{2,7}$–$8_{2,6}$) line at 102.539 GHz mainly in core #1.

The CH_3CCH spectra averaged over the beam are presented in Fig. 8. The emission from this molecule appears to be optically thin in all the cores. We overlay synthetic spectra whose parameters are indicated in Table 2. In the figure, we note the detection of an ethanol (C_2H_5OH) line at 102.534 GHz in cores #1, #2, #3, and #4, exhibiting a varying intensity from one core to the next.

Twelve CH_3CCH $v_{10} = 1$ transitions with E_u ranging from 487 to 741 K are included in the frequency range of the observations (between 102.74 and 102.94 GHz). The intensities estimated from the parameters in Table 2 are significantly below the noise level for a detection in any of the cores.

The difference in temperature between CH_3CN (120–160 K) and CH_3CCH (50–90 K) suggests that CH_3CCH traces the outer envelope whereas CH_3CN traces the inner part. Furthermore, the line width of the CH_3CCH lines compared to that of the CH_3CN lines is also smaller for each core. The observations and gas-grain chemical modelling suggest that the CH_3CN emission in IRAS 16293-2422 also arises from a warmer and more interior region of the envelope than the CH_3CCH emission (Andron et al. 2018).

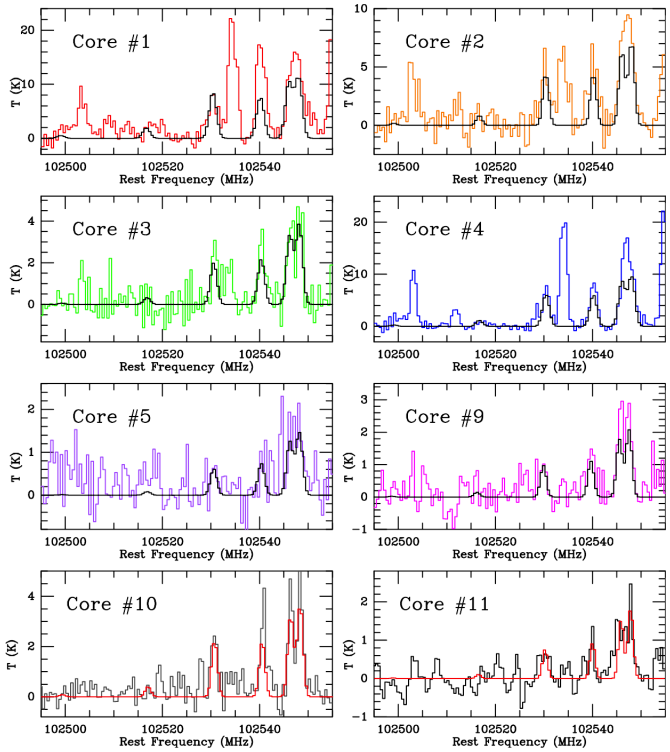

Fig. 8. CH_3CCH synthetic spectra (in red for cores #10 and #11, in black for the others) overlaid on the observed spectra. The parameters used for the synthetic spectra are listed in Table 2. The CH_3CCH lines are contaminated by an ethanol line at 102.534 GHz in cores #1, #2, #3, and #4, an ethylene glycol line at 102.539 GHz mainly in core #1, and acetone lines at 102.547 GHz in cores #1, #2, and #4.

5. Comparative molecular composition of the hot cores using methyl formate lines

5.1. Similarity of the normalised spectra

To compare the molecular composition of the selected cores, we first superposed their spectra. Because some molecular cores have much more intense lines than the others, we normalised the spectra using three bright methyl formate (CH_3OCHO, hereafter MF) doublets for this purpose; their spectroscopic parameters are listed in Table 3. The MF doublet transitions have similar E_u levels (99–109 K) and are therefore most probably tracing the same volume of gas. This strategy has the following advantages: (i) MF lines are common in all hot core spectra, (ii) easy identification of lines, (iii) lower optically thickness than for CH_3OH lines, (iv) transitions of the two torsional A– and E–species close in frequency, (v) very low contamination level of these doublets.

The spectra of each core have been aligned in velocity and multiplied by a factor so that the MF intensity of these three doublets is the same, taking core #4 as a reference. The individual velocity of the cores and the derived intensity ratio are displayed in Table 4. By applying these corrections, we obtain the superpositions shown in Fig. 9 for the six selected MF lines. The first doublet is slightly contaminated by the DCO^+ (3–2) line at 216.1126 GHz. We mapped the spatial distribution of DCO^+ emission; it is located in the high-density regions but avoids the hot cores (Molet 2019). Nonetheless, the line stands out on spectra for cores #5, #9, and #10 because the MF lines are much fainter than in the other hot cores.

Table 3. Spectroscopic parameters of the CH_3CN, CH_3CCH, and CH_3OCHO lines studied.

Transition $J=$	ν (MHz)	E_u (K)	$S\mu^2$ (D^2)	$\log(A_{ij})$ (s^{-1})
CH_3CN				
5_4–4_4	91958.73	127.5	38.2	−4.8
5_3–4_3	91971.13	77.5	135.7	−4.6
5_2–4_2	91979.99	41.8	89.0	−4.4
5_1–4_1	91985.31	20.4	101.7	−4.4
5_0–4_0	91987.09	13.2	106.0	−4.4
$CH_3^{13}CN$				
5_4–4_4	91913.35	127.5	55.4	−4.6
5_3–4_3	91925.70	77.5	196.9	−4.4
5_2–4_2	91934.53	41.8	129.2	−4.3
5_1–4_1	91939.79	20.4	147.7	−4.2
5_0–4_0	91941.58	13.2	153.8	−4.2
CH_3CN $v_8 = 1$				
$5_{1,3}$–$4_{-1,3}$	92175.52	532.3	137.3	−4.2
$5_{4,2}$–$4_{4,2}$	92218.27	705.9	51.5	−4.7
$5_{3,2}$–$4_{3,2}$	92234.54	642.6	91.5	−4.4
$5_{2,2}$–$4_{2,2}$	92247.23	593.6	240.3	−4.3
$5_{4,3}$–$4_{4,3}$	92249.65	599.4	103.0	−4.7
$5_{1,2}$–$4_{1,2}$	92256.27	558.9	137.3	−4.2
$5_{3,3}$–$4_{3,3}$	92258.43	562.8	91.5	−4.4
$5_{0,2}$–$4_{0,2}$	92261.43	538.5	143.0	−4.2
$5_{2,3}$–$4_{2,3}$	92263.98	540.4	120.1	−4.3
$5_{-1,3}$–$4_{1,3}$	92353.46	532.3	137.3	−4.2
CH_3CCH				
6_4–5_4	102516.57	132.4	55.4	−4.6
6_3–5_3	102530.35	82.0	196.9	−4.4
6_2–5_2	102540.14	46.0	129.2	−4.3
6_1–5_1	102546.02	24.4	147.7	−4.2
6_0–5_0	102547.98	17.2	153.8	−4.2
CH_3OCHO				
$19_{2,18}$–$18_{2,17}$ E	216109.78	109.3	49.4	−3.8
$19_{2,18}$–$18_{2,17}$ A	216115.57	109.3	49.4	−3.8
$19_{1,18}$–$18_{1,17}$ E	216210.91	109.3	49.4	−3.8
$19_{1,18}$–$18_{1,17}$ A	216216.54	109.3	49.4	−3.8
$17_{3,14}$–$16_{3,13}$ E	218280.90	99.7	43.6	−3.8
$17_{3,14}$–$16_{3,13}$ A	218297.89	99.7	43.6	−3.8

Notes. ν is the frequency, E_u the upper state energy, $S\mu^2$ the line strength, and A_{ij} the Einstein coefficient for spontaneous emission.

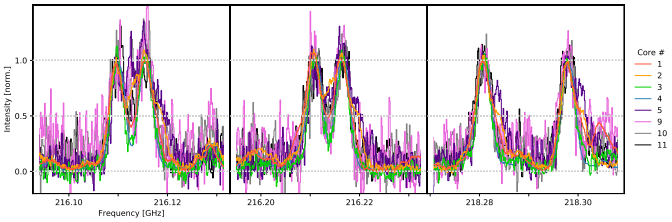

Fig. 9. Superposition of the methyl formate doublet spectra of the hot cores. The spectra are normalised with respect to the six strongest and lightly contaminated methyl formate lines. The DCO^+ (3–2) emission at 216.1126 GHz is weak with respect to the methyl formate emission towards the hot cores.

Table 4. Mass, dust temperature, velocity, and intensity scale factors of the hot cores.

Core		#4	#1	#2	#3	#5	#11	#10	#9
RA (J2000)	18^h47^m	46.98	47.02	46.84	46.37	46.76	46.52	46.91	46.48
Dec (J2000)	$-1°54'$	26.″42	26.″86	29.″30	33.″41	31.″21	24.″26	29.″99	32.″54
M_{core} ($M_\odot$)		36 ± 3	102 ± 5	55 ± 6	59 ± 2	18 ± 1	2.1 ± 0.3	16 ± 1	18 ± 1
T_{dust} (K)		88 ± 7	74 ± 2	59 ± 4	45 ± 1	47 ± 1	93 ± 11	51 ± 2	50 ± 1
v (km s^{-1})		102.3	100.2	99.2	97.2	99.0	93.9	100.8	96.4
CH_3OCHO intensity factor		1	1.2	3.1	6.6	15.4	15.5	22.8	29.1
Slope		1	0.9	2.7	7.2	16.5	11.3	28.0	32.2

Notes. The coordinates, masses, and temperatures are from M18. v is the core velocity in the local standard of rest. The CH_3OCHO intensity factors are estimated from the six lines (three doublets) of CH_3OCHO so that the intensities match those of core #4. The slope refers to the fit of Fig. 13 and is renormalised to 1 for core #4 for comparison with the CH_3OCHO intensity factor.

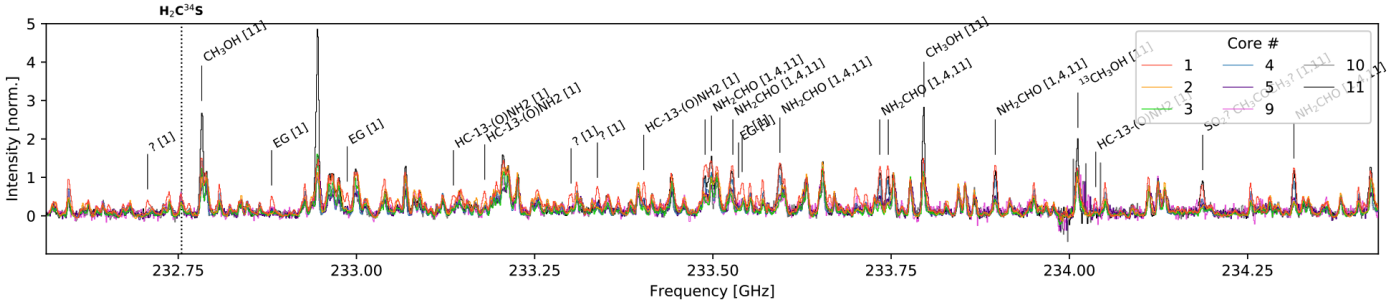

Fig. 10. Comparison of the spectra of the hot cores. The spectra are aligned in velocity and multiplied by a factor in order to normalise to a peak value of 1 for the methyl formate lines of the 216 200 and 218 200 MHz bands.

The superposition result for the Band 6 spw7 is shown in Fig. 10 and the entire spectral band superposition results are shown in Appendix A. After normalisation to the MF lines, the spectra of the eight hot cores are relatively similar. The upper level energies of the transitions are different, with a large E_u coverage for some molecules (e.g. CH_3OH, CH_3OCHO, C_2H_5CN). The fact that the intensity factor between the cores is the same for low-E_u and high-E_u transitions implies that the excitation temperatures of the cores are of the same order, which is in agreement with the results from the CH_3CN analysis (see Sect. 4).

The strongest lines come from the simplest molecules (shown as vertical dotted lines in Fig. A.1). They are associated to the following molecules: CO (and $C^{18}O$), SO, SiO, DCN, H_2CO (and $H_2^{13}CO$), HC_3N, OCS (and ^{33}S and ^{13}C isotopologues), ^{13}CS, and $H_2C^{34}S$. The study of the distribution of these molecules for core #3 showed that they are mainly not peaking at the core, except for $H_2C^{34}S$, ^{13}CS, OCS, and its isotopologues (see Molet et al. 2019; Molet 2019).

For the molecules not centred on cores, the lines are generally wider and we can see line wings associated to the outflows. A detailed study of the CO(2–1) and SiO(5–4) outflows in W43-MM1 can be found in Nony et al. (2020). A broad and bright high-velocity component for core #9, which is especially visible on the HC_3N, CO, and SO lines, is due to the presence in the projection plane of an outflow knot close to the core centre (see Fig. 3d of Nony et al. 2020). Lines are relatively intense for cores #5, #9, #10, and #11, which is probably because they are less optically thick and avoid self-absorption. A high-velocity component is visible on OCS and ^{13}CS lines for core #9.

The effect of optical thickness is visible in the line profiles of the OCS line at 231.061 GHz. If we consider that the OCS/MF ratio is the same in all the cores, the relative thickness of the OCS line for each core compared to the others is directly observable in Fig. A.1. Core #11 is the least optically thick in OCS, while cores #1 and #4 are the thickest. Furthermore, the dip at the centre of the line for these two cores confirms their strong opacity. Likewise, lines of CH_3OH and its isotopologue $^{13}CH_3OH$ in core #11 are more intense than in the other cores as they are optically thin in this core.

In the continuum spw7 band at 233 GHz, some lines are clearly more intense in the three cores #1, #4, and #11. These are all associated to NH_2CHO transitions. As E_u for these lines ranges from 94 K to 258 K, this is not an effect of temperature but can come from a larger relative abundance or a difference in the NH_2CHO emission size.

We note also that core #1 is the richest core in molecules, for example with transitions of $(CH_2OH)_2$, $H^{13}CONH_2$, and NH_2CN which are not present in the spectra of the other cores.

A c-C_3H_2 transition is detected in the core #10 spectrum at 216.278 GHz, but the spatial distribution map seems to indicate that it is mainly associated to the outflows of core #2 (see Molet 2019).

5.2. Methyl formate as a tracer of hot cores

The current understanding is that COMs, like methyl formate, mainly form through ice chemistry on grains and are then released when dust temperatures become high enough for ices to sublimate (e.g. Öberg 2016; Van Dishoeck 2017). The hot core is the inner part where the temperature is higher than ~100 K and it would be interesting to know whether or not methyl formate is a good tracer of the heating due to the luminosity of protostellar objects. All COMs do not originate from gas with the same physical conditions. Chemical differentiation (CN- vs. O-bearing molecules) has been widely observed in a great

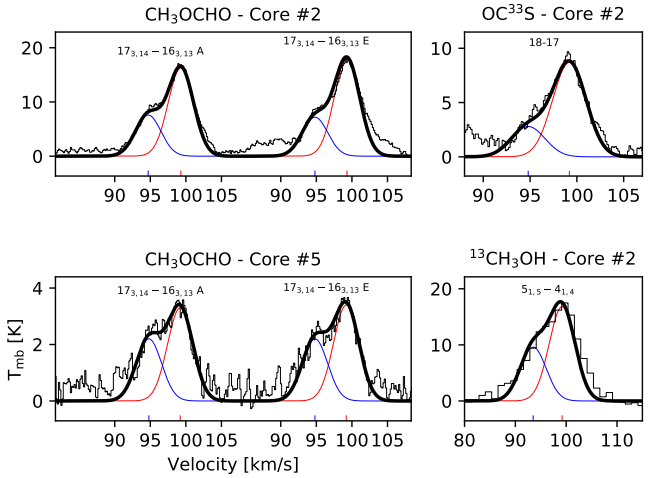

Fig. 11. Two velocity components are visible in COM lines for cores #2 and #5. For CH_3OCHO and $OC^{33}S$, the red component is at 99.2 km s^{-1} and the blue component at 94.8 km s^{-1}, with a half-power width of 4.2 km s^{-1}. For $^{13}CH_3OH$, the red component is at 99.2 km s^{-1} and the blue component at 94.7 km s^{-1}, with a half-power width of 6.0 km s^{-1}.

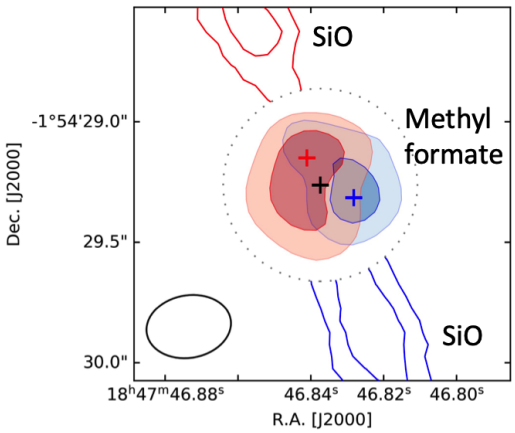

Fig. 12. Emission inside the dotted circle is the 218 GHz methyl formate doublet integrated in velocity (blue: 90–97 km s^{-1}, red: 97–104 km s^{-1}) towards core #2. The emission outside is the SiO (blue: 82–88 km s^{-1}, red: 108–119 km s^{-1}). Contours are 50% and 80% of maximum. The black ellipse is the methyl formate 0.28″ × 0.20″ beam. The black cross marks the centre of the continuum core and the red and blue crosses the maximum of the methyl formate emission.

many sources (e.g. Csengeri et al. 2019, and references therein). Towards G328.2551–0.5321, Csengeri et al. (2019) find that several O-bearing COMs peak at the proposed accretion shocks rather than at the radiatively heated core whereas CN-bearing molecules peak towards the central protostar.

In W43-MM1, at a spatial resolution of ∼2500 au, the emission of the COMs is spatially centred on the hot cores. However a clear second component of methyl formate (shifted by ∼4 km s^{-1}) is visible for cores #2 and #5 (Fig. 11). This component is also spatially centred on the continuum core and does not come from a nearby source. A second faint component may be present as well for cores #9 and #10 and a faint third component for core #5 (shifted by ∼7 km s^{-1}). These components are visible in other O-bearing molecules such as $CH_3^{18}OH$ and OCS and its isotopologues and for optically thin lines.

Figure 12 presents the spatial distribution of the blue and red components of the methyl formate lines for core #2 but at a higher resolution (0.24″ or ∼1300 au). These components do not peak at the continuum centre and their positions coincide with the blue and red parts of the outflows as traced by the CO and SiO emission (see also Fig. 3c of Nony et al. 2020). This suggests that the methyl formate emission, as well as that from the methanol and OCS, is related to the outflows and that they could have been released from the ice mantles via sublimation through shocks or UV irradiation by the protostar on the walls of the outflow cavity. The enhancement of COMs in regions of outflows is commonly observed towards high-mass (e.g. Favre et al. 2011; Palau et al. 2017) and low-mass (e.g. Drozdovskaya et al. 2015; Lefloch et al. 2017; Belloche et al. 2020; De Simone et al. 2020) protostars. If the protostellar luminosity increases, the phenomena of accretion, ejection, and shocks will be enhanced and the methyl formate emission will increase as well and can be used to trace the hot cores and the thermal heating from their embedded protostellar objects (Bonfand et al., in prep.).

6. Discussion: similarity of the molecular composition of the hot cores

6.1. General similarity of the spectra

The simple superposition of the spectra of the different cores (Fig. A.1) suggests a general similarity. If confirmed, this would point towards both a similar chemical composition and excitation of most of the COMs. A full modelling of each source in terms of physical structure and chemical composition would be the ideal approach but this is a lengthy process. We propose here a simpler, preliminary approach to start quantifying the similarity of the cores based on correlation plots of each source spectrum with that of a reference source.

The plots are presented in Fig. 13, taking core #3 as a reference. The intensity of each channel in the spectra of the different cores is plotted with respect to the intensity of the same velocity channel of core #3, after shifting the spectra with respect to the core velocities. Here we selected core #3 as a reference source, as the lines are intense but less optically thick than in core #4, which avoids biases (see Sect. 6.2). Larger circles indicate peaks in the core #3 spectrum, defined as channels above their two closest neighbours and stronger than 1 K (to remain well above the noise). The plots show a general correlation but with some dispersion, and a tendency in some cases towards a curved rather than a linear relation. The slopes of the linear fits (renormalised to 1 for core #4 for comparison) are given in Table 4 and they are plotted versus the methyl formate scaling factors in Fig. 14. It appears that the two methods for comparing the line spectra give coherent results.

Hereafter, we first discuss various causes of possible dissimilarity in the spectra and how they affect the spectrum versus spectrum plots. We then discuss the observed similarity in a more quantitative way and find an agreement within a factor 2–3.

6.2. Reasons for dissimilarity

We consider that all lines are thermalised (see Sect. 4.1). If the molecular emission of two cores is identical, the spectrum–spectrum plot should be linear, and only affected by the observational noise (5 sigma ∼1 K). Possible reasons for dissimilarity are listed below and illustrated using simulated spectra in Appendix B:

– Velocities: If the emission lines of the molecules are not centred at the same velocity in two cores, each line will appear as a loop in the diagram due to the Doppler shift. To remove this effect, we realigned each core spectrum with respect to the

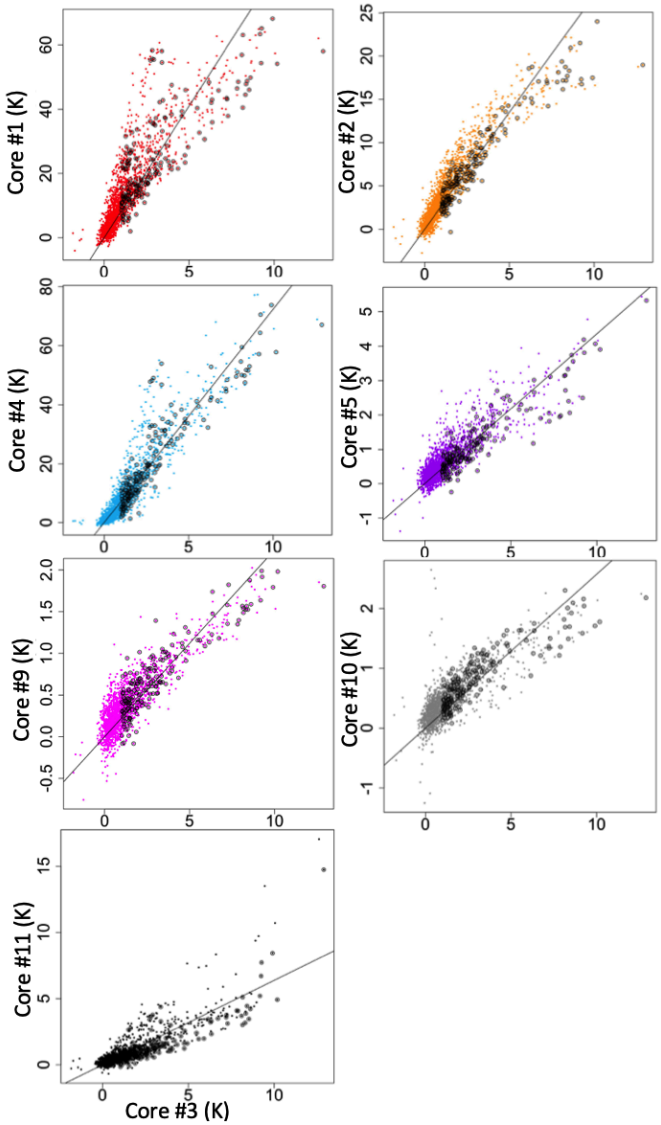

Fig. 13. Intensity of frequency channels for cores #1, #2, #4, #5, #9, #10, and #11 versus the intensity of the same frequency channel for core #3 for the spectra of the spw7 band after correction of the velocity. The circles mark the peaks of the spectra. The line is a linear fit to the point distribution.

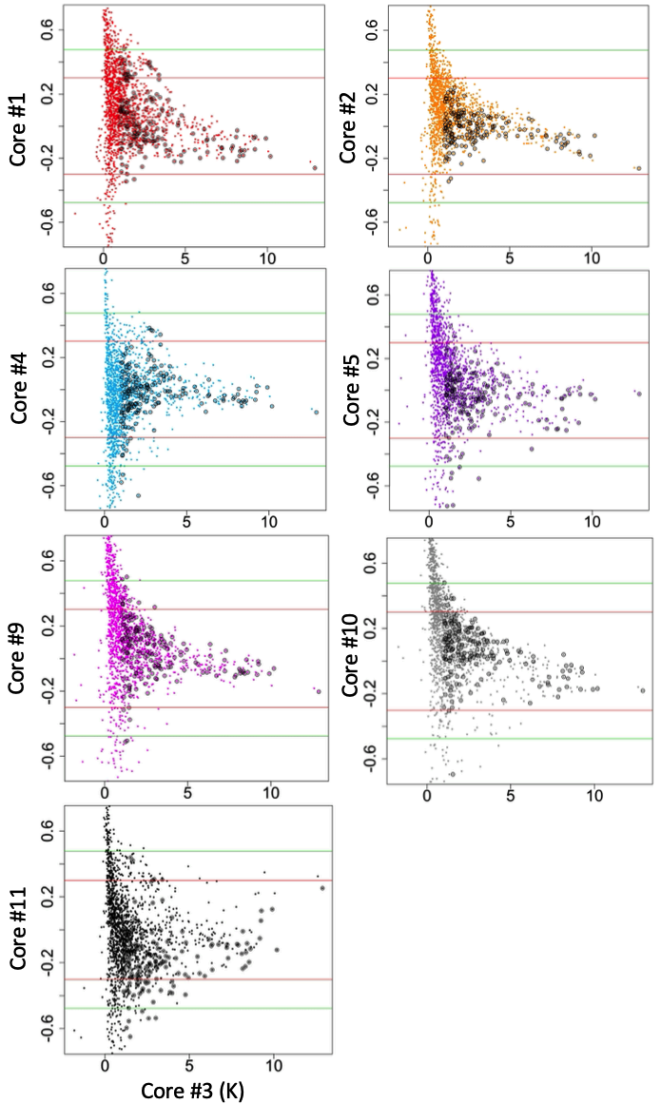

Fig. 15. Logarithm of the normalised ratio $R_i = T_i^S/(a_1 \times T_i^{S_3})$ for cores #1, #2, #4, #5, #9, #10, and #11 versus $T_i^{S_3}$, the channel intensity of the reference source core #3 (see Sect. 6.3). Horizontal red and green lines indicate a departure from $R_i = 1$ by a factor 2 and 3, respectively. Circles indicate peaks in the core #3 spectrum. Most points right of $T_i^{S_3} = 2$ K remain within a factor of 2 of the linear fit shown in Fig. 13 (slope a_1), which indicates a good general similarity in the spectra.

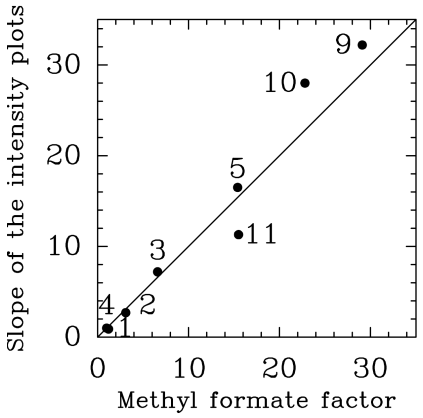

Fig. 14. Slope of the linear fit of Fig. 13 versus the methyl formate scaling factor of Fig. 10.

reference core spectrum by varying the relative velocity shift to minimise the dispersion in the spectrum–spectrum plot.

– Linewidths: a difference in line width would increase the dispersion, but here all sources have similar line widths, except core #5 (see Table 2).

– Masses: if the cores have a similar structure, but one is more massive, the relation between optically thin lines will be linear, but with a slope different from 1. The stronger lines will not be affected by optical thickness in the same way, and the line profiles will differ.

– Temperatures: if the temperature is different in the two cores, each individual optically thin line will still lead to linear relations but with different slopes for different energy levels.

– Abundances: if the relative abundance of molecules is not exactly the same, thin lines will present a linear relation but with different slopes for each species.

From an astrophysical point of view, sources in our sample differ by a factor 6 in mass for the massive cores (even up to ~50 if core #11 is included), leading to much higher column densities and opacities in some of them. Moreover, some cores might include unresolved multiple sources and some might have a noticeable proportion of molecules released by shocks (e.g. linked to bipolar flows) in addition to thermal desorption and ice sublimation. In those cases, the kinematics and the composition of the gas could be affected to some extent. However, observationally, as shown below, the molecular emission spectra of the cores are quite similar.

6.3. Similarity from ratio plots

To get a more quantitave indication of the similarity of the spectra, we plotted in Fig. 15 the logarithm of the ratio of one spectrum to the linear fit (see Fig. 13). More precisely, we define the quantity R_i for each frequency channel i as $R_i = T_i^S / (a_1 \times T_i^{S_{\rm ref}})$ where T_i^S and $T_i^{S_{\rm ref}}$ are the channel intensities, respectively, for core S and a core $S_{\rm ref}$ taken as reference, and a_1 is the slope of the linear fit (with no constant term) of T_i^S versus $T_i^{S_{\rm ref}}$. As mentioned above, the spectrum of S was first realigned in velocity with respect to the spectrum of $S_{\rm ref}$. Figure 15 presents plots of log (R_i) versus $T_i^{S_{\rm ref}}$. For all sources, R_i remains close to 1 within a factor of 3, and in many cases within a factor of 2, for most channels i where the core #3 spectrum is above 2 K (core #3 maximum intensity being about 12.9 K); these limits are indicated respectively by the green and red horizontal lines. One notes a slight decrease in the ratio R_i with $T_i^{S_3}$ which is due to opacity effects in the strongest lines. Core #11, which is the least massive, appears the least well correlated to core #3. The rather limited dispersion in the plots indicates a limited role of the potential dissimilarity factors listed above.

The agreement within a factor 2–3 between the spectra suggests a similar molecular composition of the cores, which could be due to the formation of the molecules. The lines in the spw7 band are principally those of COMs which are mainly formed on similar ices in the filament and desorbed by shocks and/or by the high temperature.

7. Conclusion

Here, we studied the molecular composition of the rich high-mass star forming region W43-MM1 with ALMA at high spatial resolution (0.5″). This study proposes analysis tools and lays the groundwork for future comparisons to similar systems.

– We developed different methods to identify the molecular hot cores. The first one relies on the continuum versus line emission separation method developed by Molet et al. (2019), which we applied to a 2 GHz band around 233 GHz that is rich in COM lines and is not contaminated by strong lines of simpler species. Hot cores are then identified in the map of the continuum-subtracted brightness temperature averaged over the band, the peaks of which highlight intense COM emission.

– A second hot core identification method uses the relative contribution of lines and continuum, but in spectra spatially averaged on previously identified continuum cores. In this case, all the nine bands we observed are used, narrow as well as broad. The criterion relies either on the summed line intensities or on the number of line channels. The results are in general agreement with the first method but some bands with strong lines of simple species are definitely less sensitive.

– We made methyl formate (CH_3OCHO) and methyl cyanide (CH_3CN) maps which highlight the same hot cores as previously determined and confirmed their nature. We also note extended methyl cyanide emission which may trace the warm gas associated with the low-velocity shocks also observed in SiO.

– Seven hot cores with 16 to 100 $M_\odot$ in mass and one less massive 2 $M_\odot$ core were identified.

– For each identified core, we determined mean temperatures using the classical 'thermometer molecules' methyl cyanide (CH_3CN) and methyl acetylene (CH_3CCH) lines at 3 mm. The $CH_3^{13}CN$ isotopologue lines allowed us to circumvent the optical thickness of the lines in the strongest sources (#1–4). CH_3CN temperatures are all consistently around 150 K, whereas CH_3CCH leads to a lower value in the 50–90 K range. This is interpreted as being due to a distribution extending further into the envelope beyond the hot core region where ice mantles have been sublimated. The previous studied core #6 is confirmed as atypical with a lower CH_3CN temperature of ~60 K.

– We compared the chemical composition of the cores using two methods. First, we directly superposed the COM-rich ~2 GHz wide spectra around 233 GHz after a scaling in intensity based on methyl formate lines. We then plotted correlation diagrams of the brightness temperature in each channel. No line identification is required. We find general good agreement, that is, to within a factor of 2–3, between the mean in the chemical composition of the various hot cores, which cover an order of magnitude in mass.

– Core #1 is especially rich in molecular lines, including ethylene glycol $(CH_2OH)_2$, formamide isotopologue $H^{13}CONH_2$, and cyanamide NH_2CN, which are not detected in other cores.

– Simpler species, such as SiO, DCN, H_2CO, CO, and SO do not have emission concentrated in the cores; but $H_2C^{34}S$, ^{13}CS, and OCS (and isotopologues) do show such concentrations.

– In core #2, we find a spatial association between the blue and red velocity components of methyl formate and the outflow lobes.

We plan to develop these studies in the frame of forthcoming analyses of the sources in the W43-MM2 and W43-MM3 ALMA-IMF regions.

Acknowledgements. We thank the anonymous referee for his helpful comments improving the manuscript. This paper makes use of the following ALMA data: ADS/JAO.ALMA#2013.1.01365.S, ADS/JAO.ALMA#2015.1.01273.S, ADS/JAO.ALMA#2017.1.01355.L. ALMA is a partnership of ESO (representing its member states), NSF (USA) and NINS (Japan), together with NRC (Canada), MOST and ASIAA (Taiwan), and KASI (Republic of Korea), in cooperation with the Republic of Chile. The Joint ALMA Observatory is operated by ESO, AUI/NRAO and NAOJ. This work is based on an analysis carried out with the CASSIS software and the CDMS and JPL spectroscopic databases. CASSIS has been developed by IRAP-UPS/CNRS (http://cassis.irap.omp.eu). This work was supported by the Programme National de Physique Stellaire and Physique et Chimie du Milieu Interstellaire (PNPS and PCMI) of CNRS/INSU (with INC/INP/IN2P3). The project leading to this publication has received support from ORP, that is funded by the European Union's Horizon 2020 research and innovation programme under grant agreement No 101004719 [ORP]. This project has received funding from the European Research Council (ERC) via the ERC Synergy Grant ECOGAL (grant 855130), from the French Agence Nationale de la Recherche (ANR) through the project COSMHIC (ANR-20-CE31-0009). A.G. acknowledges support from NSF grant AST 2008101. P.S. was partially supported by a Grant-in-Aid for Scientific Research (KAKENHI Number 18H01259) of the Japan Society for the Promotion of Science (JSPS). G.B. acknowledges support from the PID2020-117710GB-I00 grant funded by MCIN/AEI/10.13039/501100011033 and from the "Unit of Excellence María de Maeztu 2020-2023" award to the Institute of Cosmos Sciences (CEX2019-00918-M). A.S. gratefully acknowledges funding support through Fondecyt Regular (project codes 1180350 and 1220610), from the ANID BASAL project FB210003, and from the Chilean Centro de Excelencia

en Astrofísica y Tecnologías Afines (CATA) BASAL grant AFB-170002. LB gratefully acknowledges support by the ANID BASAL projects ACE210002 and FB210003. R.G.M. and T.N. acknowledge support from UNAM-PAPIIT project IN108822.

References

Andron, I., Gratier, P., Majumdar, L., et al. 2018, MNRAS, 481, 5651
Bally, J., Anderson, L. D., Battersby, C., et al. 2010, A&A, 518, A90
Belloche, A., Maury, A. J., Maret, S., et al. 2020, A&A, 635, A198
Blake, G. A., Sutton, E. C., Masson, C. R., & Phillips, T. G. 1987, ApJ, 315, 621
Carlhoff, P., Nguyen Luong, Q., Schilke, P., et al. 2013, A&A, 560, A24
Cesaroni, R., Olmi, L., Walmsley, C. M., Churchwell, E., & Hofner, P. 1994, ApJ, 435, L137
Charnley, S. B. 2011, Hot Cores, in Encyclopedia of Astrobiology, eds. M. Gargaud, R. Amils, et al. (Springer Berlin Heidelberg), 763
Cortes, P. C. 2011, ApJ, 743, 194
Cortes, P. C., Parra, R., Cortes, J. R., & Hardy, E. 2010, A&A, 519, A35
Cortes, P. C., Girart, J. M., Hull, C. L. H., et al. 2016, ApJ, 825, L15
Csengeri, T., Bontemps, S., Schneider, N., et al. 2011, ApJ, 740, L5
Csengeri, T., Belloche, A., Bontemps, S., et al. 2019, A&A, 632, A57
De Simone, M., Codella, C., Ceccarelli, C., et al. 2020, A&A, 640, A75
Drozdovskaya, M. N., Walsh, C., Visser, R., Harsono, D., & van Dishoeck, E. F. 2015, MNRAS, 451, 3836
Favre, C., Despois, D., Brouillet, N., et al. 2011, A&A, 532, A32
Giannetti, A., Leurini, S., Wyrowski, F., et al. 2017, A&A, 603, A33
Ginsburg, A., Csengeri, T., Galván-Madrid, R., et al. 2022, A&A, 662, A9
Gusdorf, A., Riquelme, D., Anderl, S., et al. 2015, A&A, 575, A98
Gusdorf, A., Anderl, S., Lefloch, B., et al. 2017, A&A, 602, A8
Herbst, E., & van Dishoeck, E. F. 2009, ARA&A, 47, 427
Herpin, F., Marseille, M., Wakelam, V., Bontemps, S., & Lis, D. C. 2009, A&A, 504, 853
Herpin, F., Chavarría, L., van der Tak, F., et al. 2012, A&A, 542, A76
Jørgensen, J. K., Belloche, A., & Garrod, R. T. 2020, ArA&A, 58, 727
Lefloch, B., Ceccarelli, C., Codella, C., et al. 2017, MNRAS, 469, L73
Louvet, F., Motte, F., Hennebelle, P., et al. 2014, A&A, 570, A15
Louvet, F., Motte, F., Gusdorf, A., et al. 2016, A&A, 595, A122
Milam, S. N., Savage, C., Brewster, M. A., Ziurys, L. M., & Wyckoff, S. 2005, ApJ, 634, 1126
Molet, J. 2019, Thesis, Université de Bordeaux, France
Molet, J., Brouillet, N., Nony, T., et al. 2019, A&A, 626, A132
Morris, M., Palmer, P., & Zuckerman, B. 1980, ApJ, 237, 1
Motte, F., Schilke, P., & Lis, D. C. 2003, ApJ, 582, 277
Motte, F., Nony, T., Louvet, F., et al. 2018, Nat. Astron., 2, 478
Motte, F., Bontemps, S., Csengeri, T., et al. 2022, A&A, 662, A8
Nguyen Luong, Q., Motte, F., Hennemann, M., et al. 2011, A&A, 535, A76
Nguyen-Luong, Q., Motte, F., Carlhoff, P., et al. 2013, ApJ, 775, 88
Nguyen-Luong, Q., Anderson, L. D., Motte, F., et al. 2017, ApJ, 844, L25
Nony, T., Louvet, F., Motte, F., et al. 2018, A&A, 618, A5
Nony, T., Motte, F., Louvet, F., et al. 2020, A&A, 636, A38
Öberg, K. I. 2016, Chem. Rev., 116, 9631
Palau, A., Walsh, C., Sánchez-Monge, Á., et al. 2017, MNRAS, 467, 2723
Pouteau, Y., Motte, F., Nony, T., et al. 2022, A&A, 664, A26
Sridharan, T. K., Rao, R., Qiu, K., et al. 2014, ApJ, 783, L31
Van Dishoeck, E. F. 2017, Proc. Int. Astron. Union, 13, 3
Vastel, C., Bottinelli, S., Caux, E., Glorian, J.-M., & Boiziot, M. 2015, in SF2A-2015: Proceedings of the Annual meeting of the French Society of Astronomy and Astrophysics, eds. F. Martins, S. Boissier, V. Buat, L. Cambrésy, & P. Petit, 313
Wink, J. E., Duvert, G., Guilloteau, S., et al. 1994, A&A, 281, 505
Zhang, B., Moscadelli, L., Sato, M., et al. 2014, ApJ, 781, 89

[1] Laboratoire d'astrophysique de Bordeaux, Univ. Bordeaux, CNRS, B18N, allée Geoffroy Saint-Hilaire, 33615 Pessac, France
e-mail: nathalie.brouillet@u-bordeaux.fr
[2] Instituto de Radioastronomía y Astrofísica, Universidad Nacional Autónoma de México, Morelia, Michoacán 58089, Mexico
[3] Univ. Grenoble Alpes, CNRS, IPAG, 38000 Grenoble, France
[4] Laboratoire de Physique de l'École Normale Supérieure, ENS, Université PSL, CNRS, Sorbonne Université, Université de Paris, Paris, France
[5] Observatoire de Paris, PSL University, Sorbonne Université, LERMA, 75014 Paris, France
[6] DAS, Universidad de Chile, 1515 camino el Observatorio, las Condes, Santiago, Chile
[7] Department of Astronomy, University of Florida, PO Box 112055, USA
[8] European Southern Observatory, Karl-Schwarzschild-Strasse 2, 85748 Garching bei München, Germany
[9] Departament de Física Quàntica i Astrofísica (FQA), Universitat de Barcelona, c/ Martí i Franquès 1, 08028 Barcelona, Spain
[10] Institut de Ciències del Cosmos (ICCUB), Universitat de Barcelona (UB), c/ Martí i Franquès 1, 08028 Barcelona, Spain
[11] Institut d'Estudis Espacials de Catalunya (IEEC), c. Gran Capità, 2-4, 08034 Barcelona, Spain
[12] Departamento de Astronomía, Universidad de Chile, Casilla 36-D, Santiago, Chile
[13] Instituto Argentino de Radioastronomía (CCT-La Plata, CONICET; CICPBA), C.C. No. 5, 1894, Villa Elisa, Buenos Aires, Argentina
[14] National Astronomical Observatory of Japan, National Institutes of Natural Sciences, 2-21-1 Osawa, Mitaka, Tokyo 181-8588, Japan
[15] Department of Astronomical Science, SOKENDAI (The Graduate University for Advanced Studies), 2-21-1 Osawa, Mitaka, Tokyo 181-8588, Japan
[16] Departamento de Astronomía, Universidad de Concepción, Casilla 160-C, 4030000 Concepción, Chile

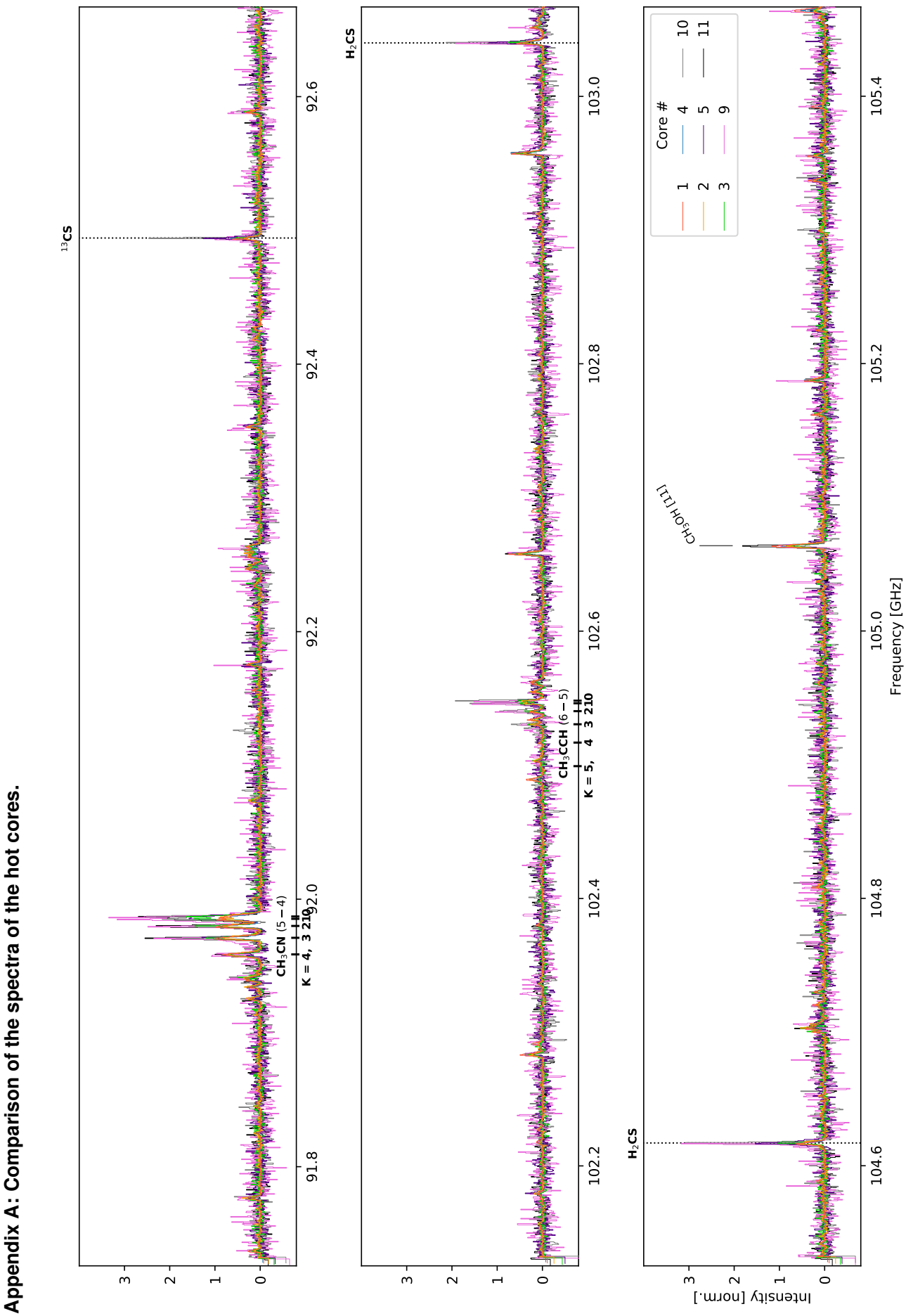

Fig. A.1: Comparison of the spectra of the eight hot cores. The spectra are aligned in velocity and multiplied by a factor in order to normalise the methyl formate lines of the 216200 and 218200 MHz bands. The hatched rectangles indicate the regions of the spectra with strong noise.

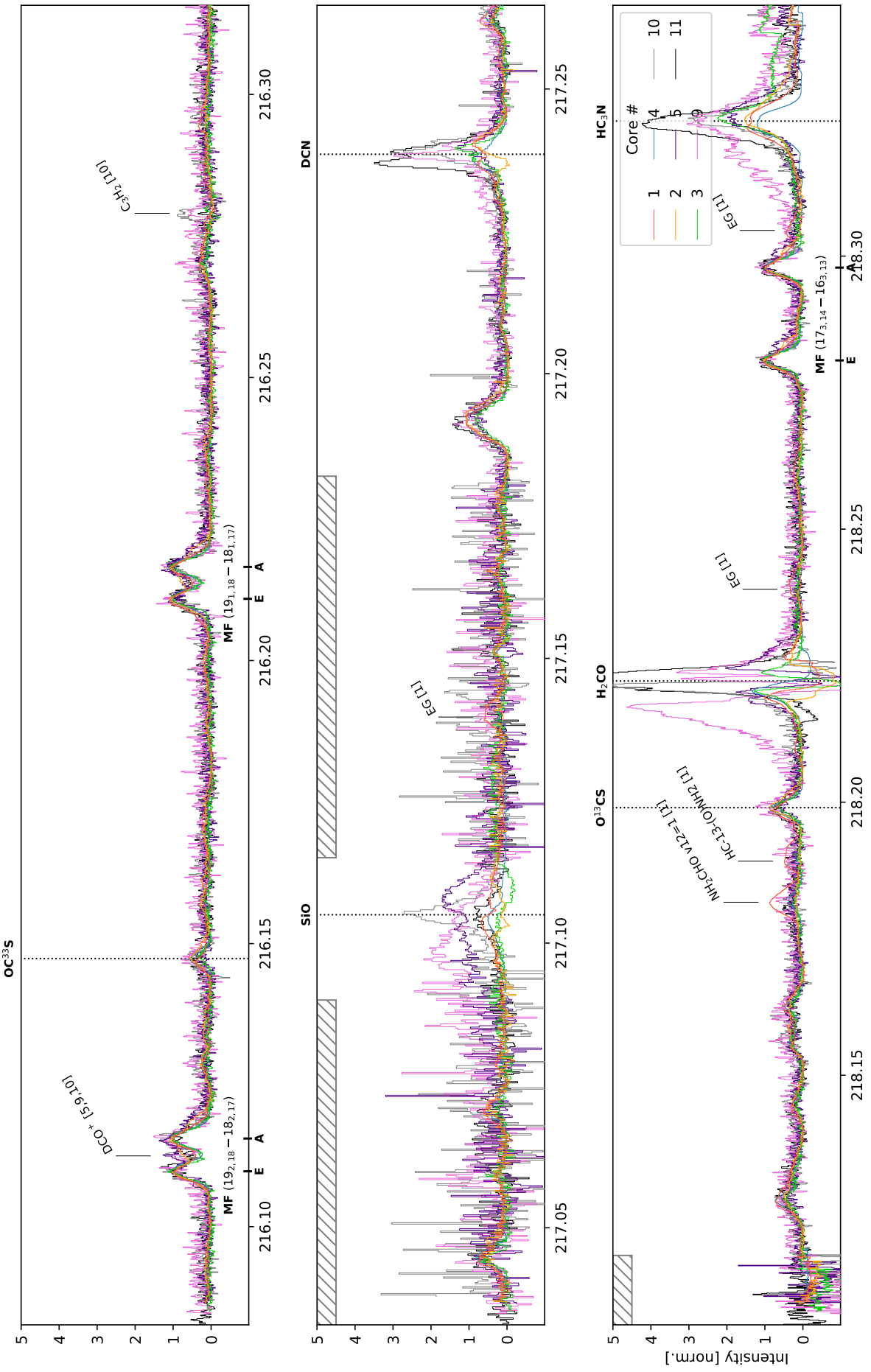

Fig. A.1: continued.

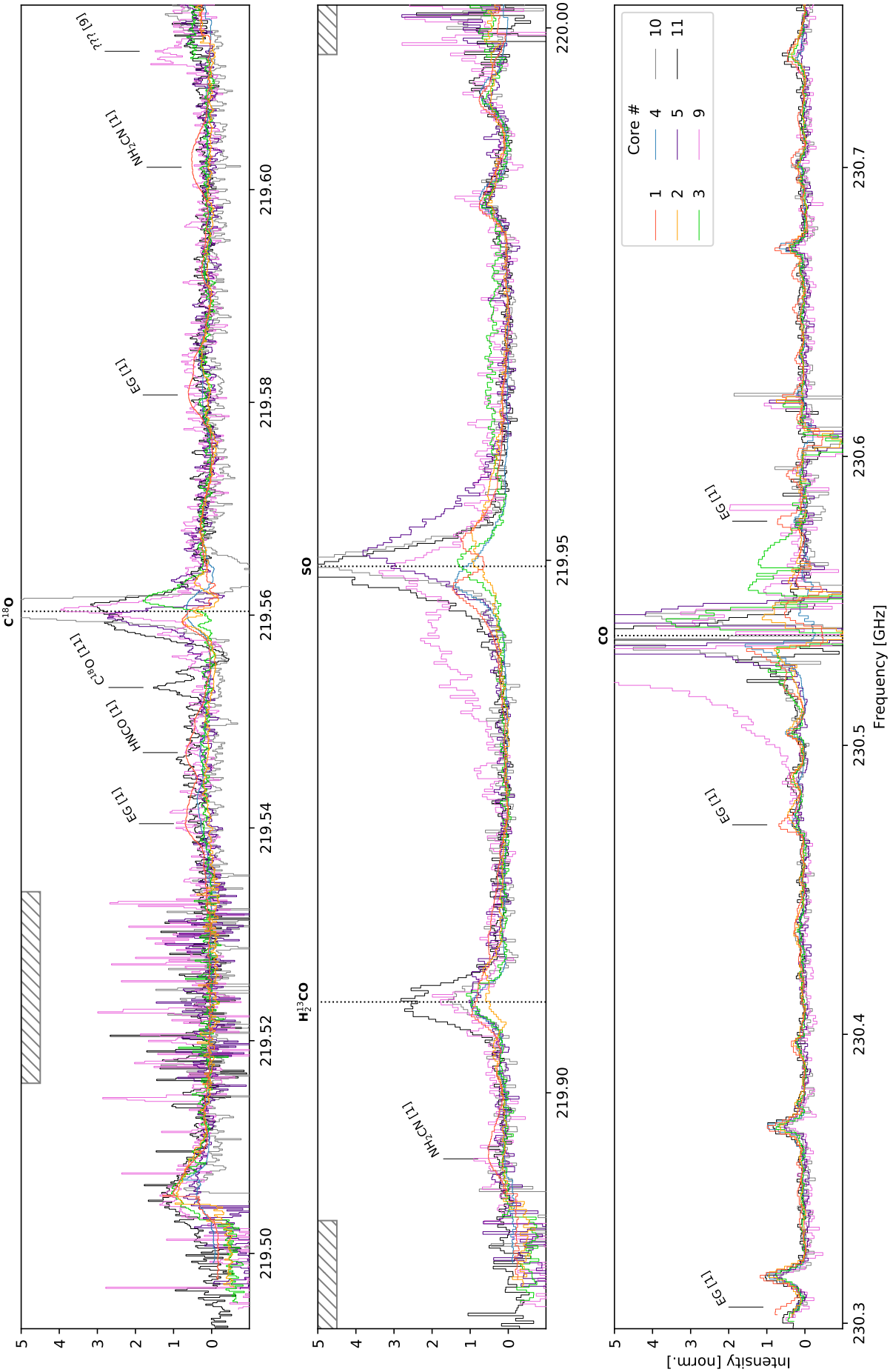

Fig. A.1: continued.

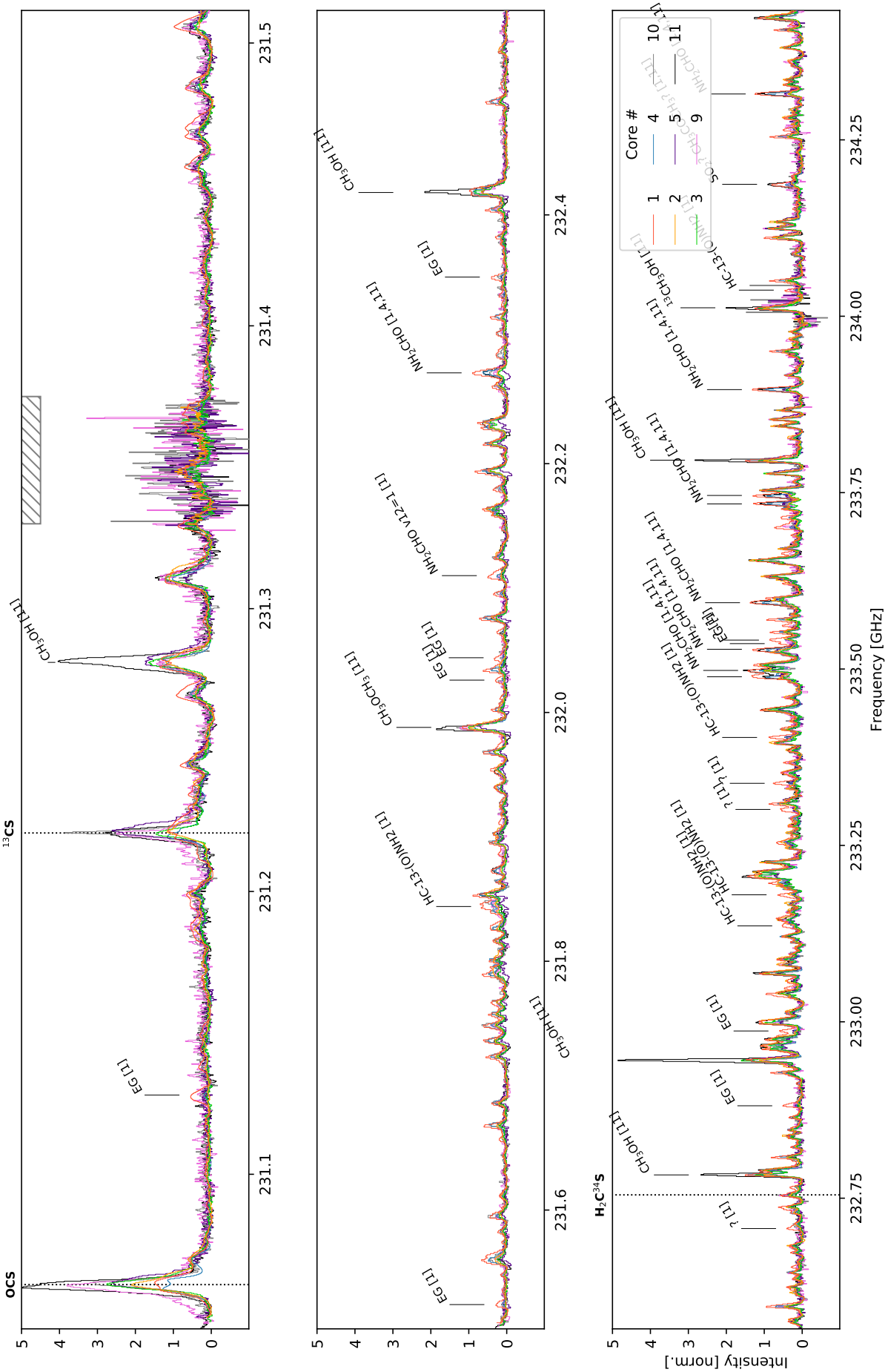

Fig. A.1: continued.

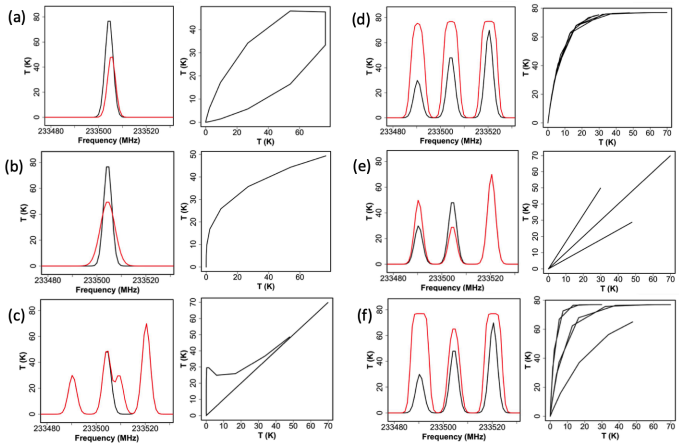

Fig. B.1: Effects of dissimilarity in the correlation plots.

Appendix B: Sources of dissimilarity in the correlation plots.

To help visualise the effects of various sources of dissimilarity discussed in Sect. 6.2 on the 'correlation' plots of Fig. 13, we provide in Fig B.1 a few examples of such plots drawn with simple synthetic spectra. These spectra are presented in the left column and the corresponding correlation plots in the right column for each case. The reference spectrum is plotted in black, and the compared spectrum in red. For optically thin lines the profile is Gaussian.

The following effects are shown:

- (a) a shift in frequency by 1 MHz (corresponding for spw7 band to about 1.3 km s^{-1});
- (b) a larger line width (9 km s^{-1} compared to 5 km s^{-1} in the reference spectrum);
- (c) spectral confusion: a line present only in the second spectrum merges partially into one of the three lines (otherwise similar in both spectra);
- (d) the lines in the second spectrum are more intense and optically thick;
- (e) the relative intensity of the three lines is different in both spectra. This mimics either a difference in abundances if the lines are from different species, or a difference in rotational temperatures if the lines are from the same species but have different upper level energies;
- (f) a combination of the two previous effects (d) and (e).

A perfect proportionality of the two spectra would lead to a single line in the correlation plots. The first effect should not be present for single-component sources, as the spectra have been realigned intentionally. All other effects would widen and/or deform the correlation. The correlation plots in Sect. 6.2 obtained with the observed spectra show that the combined effect of all these sources of dissimilarity remains limited.